Bulletin of the Seismological Society of America, Vol. 109, No. 2, pp. 732–744, April 2019, doi: 10.1785/0120180139

Ⓔ

A New Empirical Ground-Motion Model for Iran

by Z. Farajpour,* S. Pezeshk, and M. Zare

Abstract In this study, we developed a new ground-motion model (GMM) for the 5% damped horizontal spectral accelerations using a newly developed database of strong-motion records for Iran. The newly developed GMM includes peak ground acceleration and 5% damped elastic pseudospectral acceleration ordinates of 0.01 s $\le T \le$ 4.0 s. We used a database containing 1356 records from 208 events up to 2013, with the moment magnitude range of $4.8 \le \mathbf{M} \le 7.5$, and the rupture distances or closest distance to the rupture plane R_{RUP} up to 400 km. The selected database includes a variety of fault mechanisms, for example, strike slip, normal, and reverse. We used Akaike and Bayesian information to determine the validity of the chosen regression model. We introduced random-effect coefficients in our mixed-effect regression model to capture the regional variations among Zagros, Alborz–Azarbaijan, Kope Dagh, and central east Iran and found no statistical variations among these regions. As part of the developed GMMs, we included the nonlinear site effect using V_{S30} (average shear-wave velocity in the upper 30 m of soil profile). Distribution of residuals obtained considering between-event, site-to-site, and event-station showed no discernable trends for the developed GMM. Furthermore, our proposed model is compared with Kale *et al.* (2015), which has been a recent and well-established new generation model for Iran and Turkey.

Electronic Supplement: Plots of site amplification factors versus peak ground acceleration on rock ($\mathrm{PGA_{Rock}}$), variation of the between-event standard deviation τ, site-to-site standard deviation ϕ_{S2S}, within-event single-site standard deviation ϕ_{SS}, total aleatory standard deviation as a function of period, variation of site amplification factors with $\mathrm{PGA_{Rock}}$ within V_{S30} bins, and event-to-site, site-to-site, and between-event residual versus distance as a function of V_{S30} and $\mathbf{M}$ for PGA and 1 s spectral accelerations, respectively.

Introduction

This study summarizes the development of a new ground-motion model (GMM) for Iran. The Iranian plateau is a region that has continuously experienced moderate-to-large magnitude shallow earthquakes with focal depths less than 35 km and has undeniable importance for earthquake engineering studies. Furthermore, the Iranian plateau is located within the Alpine–Himalayan belt, which is one of the notable tectonically active regions in the world with strike-slip and reverse faults of frequent moderate-to-large earthquakes, with the northward Arabian plate moving toward Eurasia.

In areas of high seismicity such as the Iranian plateau, mathematical models are used to relate given ground-motion intensity measures (GMIMs) such as peak ground acceleration (PGA) and 5% damped pseudospectral accelerations (PSAs), to several seismological parameters of an earthquake such as earthquake magnitude, source-to-site distance, style of faulting (SOF), and local site conditions. The near-source GMMs are of great importance in performing engineering applications. Ground motions in Iran are characterized by active strike-slip and reverse faults, and various researchers have divided the Iranian plateau into several tectonic regions based on seismicity and geophysical characteristics. Currently, there is no consensus among researchers on how to split the Iranian plateau into various tectonic regions. Some authors proposed simplified provinces (e.g., Stoklin, 1968; Takin, 1972; Berberian, 1979; Chandra *et al.*, 1979). Interestingly, a few other researchers such as Nowroozi (1976) and Tavakoli and Ghafory-Ashtiany (1999) divided Iran into more detailed tectonic regions. Each region frequently has moderate-to-large earthquakes, and in some cases, researchers prefer to present

*Also at The University of Memphis, Department of Civil Engineering, Memphis, Tennessee.

the attenuation relationships or ground-motion prediction equations (GMPEs) for each region separately.

In this study, we considered five major seismotectonic regions based on all geophysical, geological, tectonic, and earthquake data as proposed by Mirzaei *et al.* (1998): (1) Zagros is a continental–continental collision zone of the Arabian plate and central Iranian microcontinent; (2) Alborz–Azarbaijan lies through north and northwest Iran and is part of the Alpine–Himalayan seismic belt; (3) Kope Dagh is also a segment of the Alpine–Himalayan seismic belt; (4) central-east Iran is an intraplate subjected to the foregoing convergent zones; and (5) anything not included in the above four identified regions. Zare *et al.* (1999), Nowroozi (2005), Zare and Sabzali (2006), and Ghasemi *et al.* (2009) considered a different approach and grouped the tectonic regions and developed models individually for each subset. The final attenuation curves presented by Zare *et al.* (1999) were similar for each region, and the differences appear negligible given the estimated standard deviations of the relationships. Several researchers, such as Zafarani *et al.* (2008), Soghrat *et al.* (2012), Zafarani and Soghrat (2012), and Sedaghati and Pezeshk (2017) present a GMM for specific regions with a homogenous tectonic regime. Ghasemi *et al.* (2009) and Kotha *et al.* (2016) used the analysis of the variance technique and determined that ground motions from Alborz of central Iran and the Zagros regions can be combined into one set. In this study, we introduced random-effect coefficients in our functional form to investigate the effect of the regional differences on our GMM.

In the last decade, most of the scholars have developed regional GMMs using databases that are similar to regional tectonic characterizations. Kale *et al.* (2015) present a GMM for Turkey and Iran to investigate the possible regional effects on ground-motion amplitudes in shallow active-crustal earthquakes. They used a total of 670 Turkish and 528 Iranian accelerograms with depths down to 35 km to estimate PGA, peak ground velocity, and 5% damped PSA for a period range of 0.01 s $\leq T \leq$ 4 s. They considered the moment magnitude domain between 4 and 8 and used Joyner–Boore distances up to 200 km. Kale *et al.* (2015) state that the ground-motion amplitudes of Turkey and Iran have different characteristics than the ground-motion estimates of GMMs developed from the strong-motion databases of shallow active-crustal earthquakes from other countries. Therefore, the focus of the present study is to develop a new ground-motion prediction model using a recent comprehensive database compiled for Iran by Farajpour *et al.* (2018).

Historical Development of GMMs for Iran

There are few GMMs developed for the Iranian plateau considering various databases, magnitude and distance type and ranges, and various regions within the plateau. Ramazi and Schenk (1994) developed the first empirical predictive model for Iran to estimate PGA. They used two site conditions for which they derived two separate equations, considering events with focal depths between 10 and 69 km. Ramazi and Schenk (1994) used the hypocentral metric as a mean for representing distance, which resulted in a poor fit for the M_s 7.7 Rudbar (Manjil) earthquake (Douglas, 2004). This model was followed by Zare *et al.* (1999) to estimate PGA considering 468 three-component well-recorded data (analog and digital) using moment magnitudes **M**, hypocentral distances, and the SOF. Nowroozi (2005) developed GMPEs using a database containing 279 entries from about 30 seismogenic areas across Iran, and he estimated PGA for both horizontal and vertical components. Nowroozi (2005) considered four site categories, focal depths between 9 and 73 km, moment magnitudes **M**, and epicentral distances R_{EPI}, from 2 km to nearly 250 km. The Zare and Sabzali (2006) predictive model was developed for the entire country. They used four site classes based on the fundamental frequency and separated records into four mechanisms (reverse, reverse/strike-slip, strike-slip, and unknown). Their model is based on **M** and the hypocentral distance R_{HYP}. The limitation of their equations is the lack of near-field data. Ghasemi *et al.* (2009) proposed a GMM to estimate PSA for Iran and west Eurasia from a large dataset. Ghasemi *et al.* (2009) analyzed 716 three-component accelerograms recorded during 200 earthquakes of $\mathbf{M} \geq 5$. In addition to the Iranian data, 177 three-component strong ground motion records from west Eurasia and the Kobe earthquake data were analyzed to augment the Iranian dataset. This study is followed by Sadeghi *et al.* (2010) and Saffari *et al.* (2012) who proposed ground-motion predictive models for all of Iran and Hamzehloo and Mahood (2012) for a specific zone in Iran. The Saffari *et al.* (2012) model is applicable for different faulting mechanisms, and its site functional form is in terms of the shear-wave velocity of the top 30 m of soil V_{S30}. The most recent common Iranian and Turkish GMMs were developed by Kale *et al.* (2015), Sedaghati and Pezeshk (2017), and Zafarani *et al.* (2017). Zafarani *et al.* (2017) developed empirical equations for the prediction of GMIMs using a database of 1551 Iranian earthquakes. Sedaghati and Pezeshk (2017) developed a set of GMPEs for Iran using the Iranian Strong Motion Network (ISMN) data recorded by the Building and Housing Research Center of Iran, and they used a linear term to model site response using the top 30 m of soil V_{S30}. A comprehensive list of historical GMMs developed for the Iranian region and their specific descriptions and limitations can be found in Sedaghati and Pezeshk (2017).

Selected Iranian Strong-Motion Databases and Characteristics

The database used in this study is an integrated dataset of shallow earthquake ground motions that occurred in Iran (Farajpour *et al.*, 2018). A total of 1356 three-component strong-motion records are processed from 204 events in Iran and 4 events in Turkey and Greece for moment magnitudes $\mathbf{M} \geq 4.8$ and rupture distances $R_{\mathrm{RUP}} \leq 400$ km. Unprocessed strong-motion records were obtained from the ISMN. We processed 1288 three-component records obtained from ISMN. The strong-motion data from Iran were collected from 1976 to 2013. The causative earthquake fault seismological information is applied to gain engineering parameters required for developing and employing a GMM. The strong-motion database includes site geological characterization, causative earthquake properties, fault geometry, focal mechanism, and more than one type of the distance metrics, such as the R_{EPI}, R_{HYP}, R_{RUP}, and the Joyner–Boore distance R_{JB}. For each seismic source, the source characterization and relevant earthquake scenarios (magnitude, dimension, and location) are computed. Source characterization, such as down-dip rupture width (W) and rupture area, are assumed to be rectangular, and to describe the rupture dimension requires the rupture width and length. To determine the fault geometry, the Wells and Coppersmith (1994) and the Kaklamanos *et al.* (2011) procedures were used for estimating the source characteristics describing the fault-rupture plane: the fault dip (δ), W, and the depth-to-top of the rupture (Z_{TOR}).

The majority of stations in the ISMN, similar to other networks, limited geotechnical information. Commonly, site conditions are determined using the shear-wave velocity of the topmost 30 m V_{S30}, as a variable in evaluation of empirical relationships to predict nonlinear (i.e., amplitude-dependent) amplification factors for 5% damped response spectral acceleration (SA). The Iranian sites measured V_{S30} for 500 stations out of 1047 ISMN stations. The Wald *et al.* (2004) and Wald and Allen (2007) approaches were used to classify sites using the topographic slope as a proxy to V_{S30} where we did not have measured data. A similar approach was used by the Pacific Earthquake Engineering Research Center (PEER) Next Generation Attenuation Phase 2 (NGA-West2; Bozorgnia *et al.*, 2014) and NGA-East to estimate V_{S30} for sites where there are no measured data.

For this study, we used the Farajpour *et al.* (2018) dataset. Farajpour *et al.* (2018) provide detailed information regarding the data processing and features of the database used in this study:

- 1356 three-component acceleration records are included;
- records are processed with the standard processing techniques and checked to be of high quality;
- 500 stations in Iran measured V_{S30};
- records that do not have measured V_{S30} are given estimated values using an inferred approach;
- all records that are mainshocks and aftershock records are excluded from the dataset;
- only records with rupture distances less than 400 km are included in the final 1356 dataset; and
- we considered 19 spectral periods: PGA, 0.04, 0.042, 0.044, 0.05, 0.075, 0.1, 0.15, 0.2, 0.26, 0.3, 0.4, 0.5, 0.75, 1, 1.5, 2, 3, and 4 s.

Functional Form of the GMM

Selecting an appropriate functional form is the important step in developing and calibrating GMMs. The present study concentrates on empirical predictive equations that were developed as part of the NGA-West2 project (Bozorgnia *et al.*, 2014) conducted by PEER. In particular, we started a trial functional form similar to Campbell and Bozorgnia (2013) that showed reasonable characterization of GMMs for the Iranian plateau. We used the nonlinear mixed-effect algorithm developed by Lindstrom and Bates (1990) and employed in MATLAB (MathWorks Inc., 2017) with the functions of "nlmefit" and "fitlmematrix" (MathWorks Inc., 2017), a main approach to calibrate coefficients. This study also considered regional variations in the random-effect part of the mixed-effect regressions as well. We compared Akaike and Bayesian information criteria (AIC and BIC, respectively) values and the logarithms of their likelihoods to find an appropriate functional form that can best fit the data.

Al Atik *et al.* (2010) proposed the following nonlinear regression model to represent a mixed-based GMPE:

$$\ln(Y) = f(X_{\mathrm{es}}, \theta) + \Delta B + \Delta W, \tag{1}$$

in which $\ln(Y)$ is the natural logarithm of the observed ground-motion parameter, $f(X_{\mathrm{es}}, \theta)$ is the GMM, X_{es} is a vector of independent variables including the earthquake magnitude and the source-to-site distance, and e and s subscripts stand for an observation for earthquake e recorded at station s, respectively. The parameter θ is a vector of fixed effects for regression coefficients. ΔB is the between-event (interevents) variability, which represents the difference between the average level of ground motion for an event and the expected level for that event, and ΔW is the within-event (intraevents) variability, which represents the difference between the observed ground motion and the median ground motion for a given event (Abrahamson *et al.*, 2014). The random effects and the random error are normally distributed with zero means. Based on the considerations discussed, we propose the following functional form for this study:

$$\ln(Y) = f_{\mathrm{source}} + f_{\mathrm{path}} + f_{\mathrm{site}} + \delta B_e + \delta S_{S2S} + \varepsilon, \tag{2}$$

in which $\ln(Y)$ is the natural logarithm of the GMIM of interest (PGA and 5% damped PSAs in g). Following the Al Atik *et al.* (2010) notation, δB_e and δ_{S2S} are random effects to describe the between-event and site-to-site residuals. δB_e has a normal distribution with zero mean and standard deviation of τ. δ_{S2S} has a normal distribution with zero mean and standard deviation of ϕ_{S2S} (Al Atik *et al.*, 2010). ε is the event-site-corrected residual having normal distribution with zero mean and standard deviation of ϕ_0. f_{source}, f_{path}, and f_{site} are the source, the path, and the site functions, respectively. In the following, we discuss each term in detail.

The source function is given by

$$f_{\mathrm{source}} = f_{\mathrm{magnitude}} + f_{\mathrm{SOF}} + f_{\mathrm{dip}} + f_{\mathrm{hyp}}, \tag{3}$$

in which the median GMM is based on the geometric mean of the horizontal ground motions as a function of scaling of ground motion with respect to earthquake magnitude

$f_{\text{magnitude}}$, style of faulting f_{SOF}, dip angle f_{dip}, and hypocentral depth f_{hyp}. In this study, we did not consider the hanging-wall geometry. Each of these terms is discussed next.

Magnitude

The magnitude-scaling term includes a bilinear model and a quadratic term. The magnitude term is defined as

$$f_{\text{magnitude}} = \begin{cases} z_1 + z_2(\mathbf{M} - \mathbf{M}_{\text{h}}) + z_3(\mathbf{M} - \mathbf{M}_{\text{h}})^2; & \mathbf{M} \le \mathbf{M}_{\text{h}} \\ z_1 + z_4(\mathbf{M} - \mathbf{M}_{h}) + z_3(\mathbf{M} - \mathbf{M}_{\text{h}})^2; & \mathbf{M} > \mathbf{M}_{\text{h}} \end{cases}, \tag{4}$$

in which $\mathbf{M}$ is the moment magnitude and $\mathbf{M}_{\text{h}}$ is the hinge magnitude fixed at 6.5, and z_1–z_4 are fixed-effect coefficients. In this study, magnitude domain in our database is $4.8 \le \mathbf{M} \le 7.5$. Abrahamson *et al.* (2014) had a similar functional form, and they estimated the bilinear coefficients (z_2 and z_4) for the PGA and then constrained them to be independent of period to develop a smooth model as a function of spectral period. We obtained all fixed-effect coefficients as a function of period. Furthermore, a key feature of magnitude scaling is the degree of saturation with magnitude at short distances (Abrahamson *et al.*, 2014). Magnitude saturation represents the decreasing of ground motion with increasing magnitude. We did not constrain the coefficient z_4 to be nonnegative to allow capturing the oversaturation effect with magnitude if it exists in the dataset.

Geometric Attenuation

The path term is separated into two components, commonly referred to as geometric attenuation and anelastic attenuation. However, the behaviors of both in distance $R_{\text{RUP}} \le 80$ km are the same. In this study, we separate the effects of geometric attenuation to avoid a trade-off with anelastic attenuation. Geometric attenuation models the amplitude decay due to the expanding surface area of the wavefront as it propagates away from the source. The geometric attenuation term is defined as

$$f_{\text{geometric}} = (z_5 + z_6\mathbf{M}) \ln\left(\sqrt{R_{\text{RUP}}^2 + z_7^2}\right). \tag{5}$$

R_{RUP} is the rupture distance, and z_5, z_6, and z_7 (fictitious depth) are fixed-effect coefficients.

Style of Faulting

Kotha *et al.* (2016) and Sedaghati and Pezeshk (2017) did not identify significant differences between strike-slip and reverse mechanisms (p-values revealed that they are statistically insignificant). However, in this study, we included an f_{SOF} term in the functional form as the following:

$$f_{\text{SOF}} = c_8 f_{\text{RV}} + c_9 f_{\text{NM}}. \tag{6}$$

f_{RV} is an indicator variable representing reverse and reverse-oblique faulting, in which $f_{\text{RV}} = 1$ for $30° < \lambda < 150°$ and $f_{\text{RV}} = 0$, otherwise. f_{NM} is an indicator variable representing normal and normal-oblique faulting, in which $f_{\text{NM}} = 1$ for $-150° < \lambda < -30°$ and $f_{\text{NM}} = 0$; otherwise. A similar form was used by Campbell and Bozorgnia (2013).

Hypocentral Depth

We used a hypocentral depth term similar to the one proposed by Campbell and Bozorgnia (2013). We used a hinge magnitude point of 6.5 as shown by the data. Moreover, the following form represents the hypocentral depth term:

$$f_{\text{hyp}} = f_{\text{hyp},H} f_{\text{hyp},M}$$
$$f_{\text{hyp},H} = \begin{cases} 0; & Z_{\text{HYP}} \le 7 \\ Z_{\text{HYP}} - 7; & 7 < Z_{\text{HYP}} \le 20 \\ 13; & Z_{\text{HYP}} > 20 \end{cases}$$
$$f_{\text{hyp},M} = \begin{cases} z_{10} + (z_{11} - z_{10})(\mathbf{M} - 6.5); & \mathbf{M} \le 6.5 \\ z_{11}; & \mathbf{M} > 6.5 \end{cases}, \tag{7}$$

in which Z_{HYP} (km) is the hypocentral depth of the earthquake.

Rupture Dip

Commonly, the recordings from small magnitude earthquakes show a strong dependence on the dip of the rupture plane (Campbell and Bozorgnia, 2013). The effect is captured by a rupture dip term and model coefficient z_{12}. We defined the rupture dip term as

$$f_{\text{dip}} = \begin{cases} z_{12}\delta; & \mathbf{M} \le \mathbf{M}_{\text{h1}} \\ z_{12}(5.5 - \mathbf{M})\delta; & \mathbf{M}_{\text{h1}} < \mathbf{M} \le \mathbf{M}_{\text{h2}} \\ 0; & \mathbf{M} > \mathbf{M}_{\text{h2}} \end{cases}, \tag{8}$$

in which $\mathbf{M}_{\text{h1}} = 4.0$ and $\mathbf{M}_{\text{h2}} = 8.5$ are hinge magnitude points, and δ (°) is the average dip of the rupture plane.

Anelastic Attenuation

As mentioned earlier, the path attenuation is separated into two components, commonly referred to as geometric attenuation and anelastic attenuation. The anelastic attenuation models the amplitude decay due to the conversion of elastic wave energy to heat and usually is found to be frequency dependent. The ground-motion behavior beyond 80 km is strongly controlled by regional attenuation. The anelastic attenuation term is defined as

$$f_{\text{atn}} = \begin{cases} (z_{13} - \Delta z_{13})(R_{\text{RUP}} - 80); & R_{\text{RUP}} > 80 \\ 0; & R_{\text{RUP}} \le 80 \end{cases}. \tag{9}$$

As there is a trade-off between the geometric spreading and the anelastic attenuation terms because of the scatter of data, we constrained the coefficient z_{13} to be negative or zero. To consider the regional differences, we used a random effect represented by Δz_{13} in our mixed-effect regression model.

Table 1
Regression Coefficients z_1–z_9

T (s)	z_1	z_2	z_3	z_4	z_5	z_6	z_7	z_8	z_9
$\mathrm{PGA_{Rock}}$	1.3532	0.5437	−0.1489	1.147	−0.739	−0.0582	11.8246	0.0965	0.0136
PGA	0.6755	0.362	−0.1889	1.0966	−0.8165	−0.0189	6.1175	0.0829	0.0008
0.0400	0.9298	0.1165	−0.1944	1.0609	−1.0658	0.0052	6.9438	0.1049	0.0297
0.0420	0.9749	0.0967	−0.1905	1.0305	−1.1055	0.0103	7.0195	0.1063	0.02
0.0440	1.0408	0.1188	−0.1782	1.0308	−1.1043	0.0085	6.999	0.1131	0.0127
0.0500	1.2242	0.1259	−0.1679	1.0342	−1.1286	0.0088	6.9802	0.1092	−0.0176
0.0750	1.66	0.0212	−0.192	0.9548	−1.181	0.0076	7.9789	0.14	−0.0747
0.1000	2.0911	0.0992	−0.2315	1.053	−0.9284	−0.0408	9.6673	0.1452	−0.0817
0.1500	2.0353	0.3265	−0.2677	1.2345	−0.5399	−0.0953	9.9547	0.1376	−0.0854
0.2000	1.8916	0.6147	−0.2189	1.2388	−0.3386	−0.1172	9.9145	0.0752	−0.1339
0.2600	1.6678	0.5766	−0.2461	1.1239	−0.4767	−0.0882	9.3351	0.0653	−0.099
0.3000	1.528	0.5608	−0.2253	0.9742	−0.6159	−0.0625	8.5564	0.0598	−0.0667
0.4000	0.9768	0.4991	−0.3047	1.0477	−0.5605	−0.0564	7.2139	0.0329	−0.1425
0.5000	0.6189	0.2368	−0.4144	1.0003	−0.7503	−0.0186	6.2354	0.006	−0.124
0.7500	−0.0155	0.0406	−0.5258	1.0279	−0.9273	0.0181	4.891	0.0135	−0.0489
1.0000	−0.5112	−0.0313	−0.591	1.0189	−1.0528	0.0444	3.7002	0.0571	−0.0505
1.5000	−1.0965	0.0807	−0.5343	0.9274	−1.1721	0.0648	2.5564	0.1053	−0.0635
2.0000	−1.5241	−0.0773	−0.597	0.8714	−1.2985	0.0861	2.4747	0.1032	−0.101
3.0000	−1.9509	−0.033	−0.689	0.974	−1.1284	0.0588	2.5339	0.0619	−0.2605
4.0000	−2.1397	0.2709	−0.6354	1.1372	−0.9529	0.0266	4.4598	0.0573	−0.4473

PGA, peak ground acceleration.

The random effect represents the differences among the five regions discussed earlier. We analyzed residuals considering random-effect regression to see if we obtain statistically significant differences in the random-effect coefficient for the five regions discussed earlier. The statistical analysis indicated that there are no statistically significant differences in a typical anelastic attenuation or Q with various regions. Similar conclusions were made by Ghasemi *et al.* (2009), Kotha *et al.* (2016), and Sedaghati and Pezeshk (2017).

Shallow Site Response

We followed the parametric model of the nonlinear amplification factors that are functions of PGA on rock and V_{S30} proposed by Walling *et al.* (2008). Campbell and Bozorgnia (2013) evaluated the model developed by Kamai *et al.* (2013) that is a revised version of Walling *et al.* (2008) using the Silva (2005) 1D simulations supplemented by additional simulations for soft sites. Campbell and Bozorgnia (2013) determined that Walling *et al.* (2008) fitted their empirical data better. They used the Walling *et al.* (2008) approach to handle linear and nonlinear site responses due to available data. Following Walling *et al.* (2008) and Campbell and Bozorgnia (2013), we used the following functional form for the site term:

$$f_{\mathrm{site}} = \begin{cases} z_{14}\ln\left(\frac{V_{S30}}{k_1}\right) + k_2\left\{\ln\left[\mathrm{PGA_{Rock}} + c\left(\frac{V_{S30}}{k_1}\right)^n\right] - \ln[\mathrm{PGA_{Rock}} + c]\right\}; & V_{S30} \le k_1 \\ (z_{14} + k_2 n)\ln\left(\frac{V_{S30}}{k_1}\right); & V_{S30} > k_1 \end{cases}, \qquad (10)$$

in which $\mathrm{PGA_{Rock}}$ (g) is the median predicted value of PGA on rock, k_i are period-dependent, theoretically constrained model coefficients, $c = 1.88$ and $n = 1.18$ are period-independent, theoretically constrained model coefficients, and z_{14} is a fixed-effect coefficient. The nonlinear site-term nonlinear model coefficients k_1, k_2, n, and c by Silva (2005) were used to constrain the functional form.

To determine $\mathrm{PGA_{Rock}}$, we first separated the database and selected events that were recorded on stations with V_{S30} of 760 m/s and higher. We used a mixed-effect regression and determined all regression coefficients and ignored the site term. The regression coefficients for the $\mathrm{PGA_{Rock}}$ are provided in Table 1, which provides coefficients z_1–z_{13}. These coefficients and equations (1)–(7) are used to determine the $\mathrm{PGA_{Rock}}$ for the next phase of the regression to find z_1–z_{14} for all site conditions for PGA and spectral values. Figure 1 shows the decay of $\mathrm{PGA_{Rock}}$ amplitude as a function of rupture distance for moment magnitudes 4, 5, 6, 7, and 8.

Previous GMMs developed for Iran all used the linear part of the functional form and did not include the nonlinear site amplification effects, citing the deficient number of records with high moment magnitude and short distances. In this study, we considered both the linear and nonlinear terms. There are differences between the linear and nonlinear site-response predictions based on soil type, especially for large magnitude and close distances, which are important

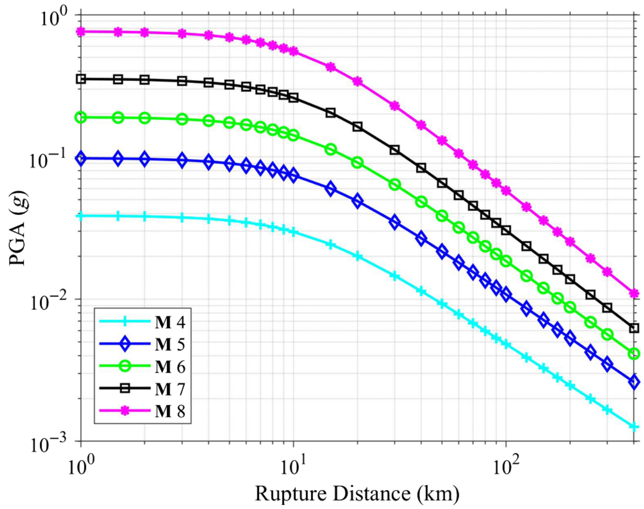

Figure 1. Attenuation of peak ground acceleration (PGA_{Rock}) as a function of rupture distance for reference rock ($V_{S30} = 760$ m/s). The color version of this figure is available only in the electronic edition.

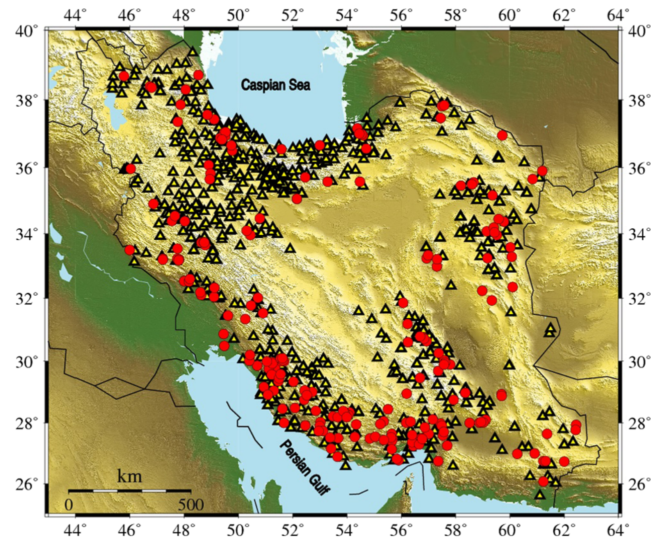

Figure 2. Distribution of recording stations and earthquakes used. Stations with determined site velocity are shown by triangle symbols. Earthquake epicentral locations are shown by circles. The color version of this figure is available only in the electronic edition.

for soft soils sites. The inclusion of the linear and nonlinear component of the ground motion in site-response analysis can significantly influence the acceleration response. Based on mixed-effect analyses, and based on our data, we have a slightly different regression coefficient than Campbell and Bozorgnia (2013). If the linear term is considered, the amplification for large rock PGA will be 1.

Ⓔ Figures S1 and S2 (available in the electronic supplement to this article) display a comparison between the nonlinear site amplification factors and the linear site amplification factors. Ⓔ Figure S1 shows a comparison of the linear site amplification, the nonlinear site amplification based on this study, as well as the nonlinear site amplification factor proposed by Campbell and Bozorgnia (2013) for V_{S30} of 560 for a spectral period of 0.2 s. This figure clearly shows that there are major differences between the linear and the nonlinear site-response amplifications. Ⓔ Figure S2 shows the differences among the linear term versus the full nonlinear site term for two V_{S30} values of 270 and 560 m/s as a function of PGA_{Rock} for a period of 0.2 s.

To show that the data have been collected and used to show a nonlinear response, we generated two figures. Ⓔ Figure S3 shows the variation of the between-event standard deviation τ, the site-to-site standard deviation ϕ_{S2S}, the within-event single-site standard deviation ϕ_{SS}, and total aleatory standard deviation as a function of period for both linear and nonlinear amplification models. This figure shows that variability is less when a nonlinear is used. Ⓔ Figure S4 was generated similar to Seyhan and Stewart (2014), which shows the within-event residuals plotted according to the predicted PGA_{rock} for several site classes and for PGA, 0.2, 1.0, and 2.0 s SAs. These two figures show that the data constrain the nonlinear part of the model.

Summary and Results

We used the nonlinear mixed-effect algorithm developed by Lindstrom and Bates (1990) and employed in MATLAB with the functions of "nlmefit" and "fitlmematrix" (MathWorks Inc., 2017), a main approach to calibration of coefficients and regional variations that are considered in the random-effect part as well. We compared AIC and BIC values and the logarithms of their likelihoods to find an appropriate functional form to best fit the data. The functional form regression coefficients obtained using a mixed-effect procedure are provided in Tables 1 and 2. Coefficients k_1 and k_2 (similar to Campbell and Bozorgnia, 2013) are also tabulated in Table 2 for completeness.

The GMIM predictions from the GMM developed in the present are compared with the PGA and PSA values from a database developed by Farajpour *et al.* (2018) for recordings with $\mathbf{M} \geq 4.8$ and $R_{RUP} < 400$ km. Figure 2 displays a map of the recording stations and earthquake events within Iran that were used for this study. Figure 3 illustrates the distribution of moment magnitudes versus the rupture distances of the selected data. Figure 3 also illustrates the distribution of datasets in terms of soil conditions (distribution of V_{S30}). All records are plotted as magnitude versus distance. We used the National Earthquake Hazards Reduction Program (NEHRP; Building Seismic Safety Council [BSSC], 2009) site classification. The Standard 2800 is the Iranian design code, and it does not have similar site classification schemes. The database is dispersed throughout all NEHRP classes. The vast majority of sites in the database are NEHRP site classes B (760 m/s $\leq V_{S30} <$ 1500 m/s) and C (360 m/s $\leq V_{S30} <$ 760 m/s), as presented.

Figures 4 and 5 display the magnitude-scaling characteristics of the PSA predicted by our central and eastern North

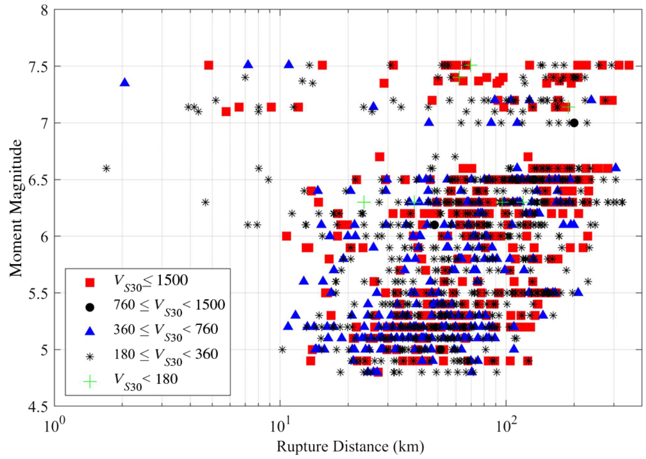

Figure 3. Magnitude versus distance of selected events considered in this study. Various markers represent the V_{S30} of each event. The color version of this figure is available only in the electronic edition.

America GMM for $R_{\mathrm{RUP}} = 10$, 75, and 120 km, and V_{S30} of 760 and 360 m/s, respectively. These figures show that the developed GMM does not exhibit much oversaturation at large magnitudes, short distances, and short periods. Because the consensus among engineering seismologists is to preclude oversaturation in GMMs (e.g., see Campbell and Bozorgnia, 2013; Abrahamson *et al.*, 2014), our approach seems reasonable. Similar behavior can be observed considering V_{S30} of 760 and 360 m/s.

There are two types of uncertainties considered when performing seismic-hazard studies: epistemic and aleatory. Aleatory uncertainty is the variability that results from the natural physical process. Epistemic uncertainty results from a lack of knowledge about earthquakes and their effects. Aleatory uncertainties are implemented directly into probabilistic seismic-hazard assessment, and epistemic uncertainties are typically considered by incorporating several models in a logic tree.

Following the Al Atik *et al.* (2010) notation, the ergodic sigma of the GMMs is typically defined as

$$\sigma_{\mathrm{ergodic}} = \sqrt{\tau^2 + \phi^2}, \tag{11}$$

in which τ is the between-event standard deviation and ϕ is the within-event standard deviation. The within-event residual can be decomposed into the site-to-site residual (δ_{S2S}) and the site- and event-corrected residual (δWS_{es}). The standard deviations of the δWS_{es} and δ_{S2S} are represented by ϕ_{SS} and ϕ_{S2S}, such that

$$\phi^2 = \phi_{SS}^2 + \phi_{S2S}^2. \tag{12}$$

Equation (11) can be rewritten as

$$\sigma_{\mathrm{ergodic}} = \sqrt{\tau^2 + \phi_{SS}^2 + \phi_{S2S}^2}. \tag{13}$$

A mixed-effect model variance-component technique was used to decompose the prediction error of the GMIMs into three components that using the terminology of Al Atik *et al.* (2010), are (1) the between-event standard deviation τ, (2) the site-to-site standard deviation ϕ_{S2S}, and (3) the within-event single-site standard deviation ϕ_{SS}. Figure 6 displays these residuals as a function of period. As can be seen in Figure 6, the total residual errors are significantly reduced

Table 2
Regression Coefficients z_{10}–z_{14}, Δz_{13}, k_1, and k_2

T (s)	z_{10}	z_{11}	z_{12}	z_{13}	z_{14}	k_1(m/s)	k_2	Δz_{13}
$\mathrm{PGA_{Rock}}$	−0.0355	−0.0676	−0.0031	0				
PGA	−0.0291	−0.061	−0.0025	0	1.4323	865	−1.186	0
0.0400	−0.0245	−0.0661	−0.0034	0	1.5027	865	−1.186	0
0.0420	−0.0251	−0.0665	−0.0034	0	1.5463	865	−1.219	0
0.0440	−0.0252	−0.0666	−0.0034	0	1.6095	908	−1.273	0
0.0500	−0.0268	−0.0656	−0.0031	0	1.7041	1054	−1.346	0
0.0750	−0.0329	−0.0687	−0.0035	0	1.8662	1086	−1.471	0
0.1000	−0.0448	−0.0754	−0.0041	−0.0013	2.0431	1032	−1.624	0
0.1500	−0.0389	−0.0775	−0.0042	−0.0011	2.3308	878	−1.931	0
0.2000	−0.0325	−0.0728	−0.0035	−0.0006	2.6048	748	−2.188	0
0.2600	−0.0278	−0.0555	−0.0023	−0.0009	2.7557	654	−2.381	0
0.3000	−0.027	−0.0431	−0.0014	−0.0015	2.8993	587	−2.518	0
0.4000	−0.0296	−0.0392	−0.0013	−0.0014	2.9942	503	−2.657	0
0.5000	−0.0384	−0.0343	−0.0009	−0.0013	2.9821	457	−2.669	0
0.7500	−0.0384	−0.0246	−0.0009	0	2.6478	410	−2.401	0
1.0000	−0.0298	−0.007	−0.0005	0	2.1147	400	−1.955	0
1.5000	−0.0442	−0.0157	−0.0021	0	0.9805	400	−1.025	0
2.0000	−0.0677	−0.0311	−0.0038	0	0.1017	400	−0.299	0
3.0000	−0.0843	−0.0349	−0.005	0	−0.2572	400	0	0
4.0000	−0.0837	−0.0359	−0.005	0	−0.2505	400	0	0

PGA, peak ground acceleration.

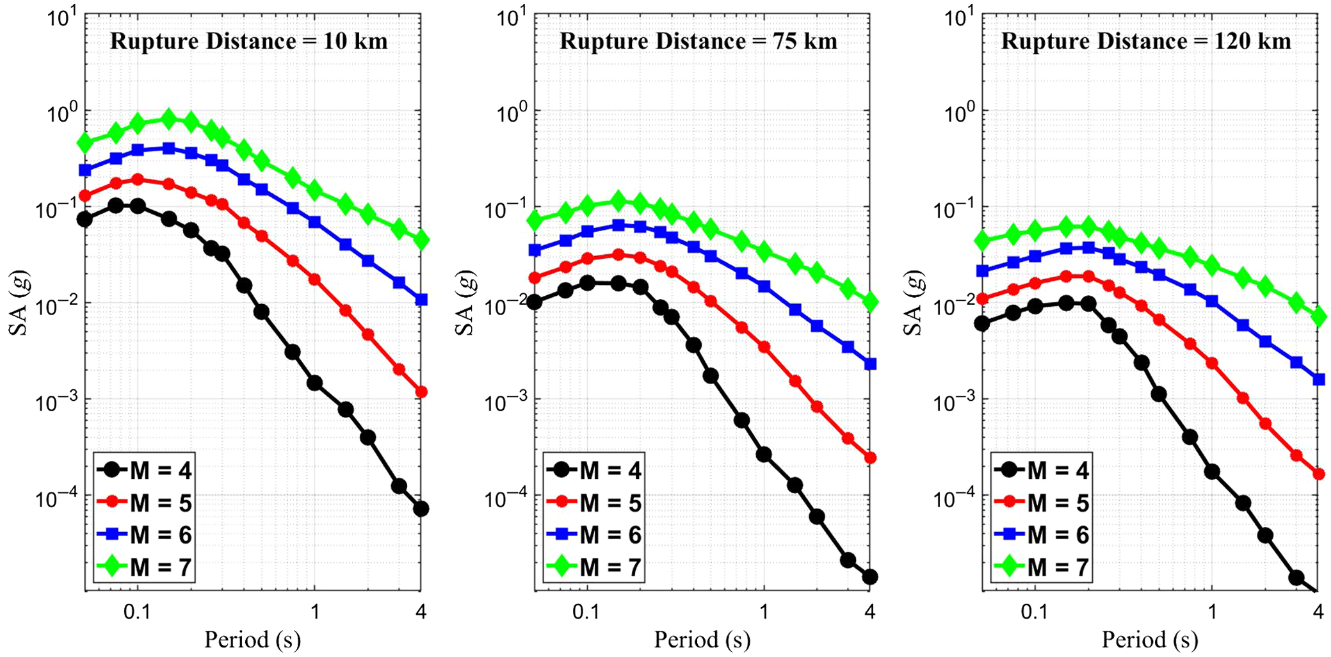

Figure 4. Response spectra predicted by the empirical ground-motion prediction equation (GMPE) developed in this study showing its dependence on magnitude at rupture distances (R_{RUP}) of 10, 75, and 120 km, considering $V_{S30} = 760$ m/s. SA, spectral acceleration. The color version of this figure is available only in the electronic edition.

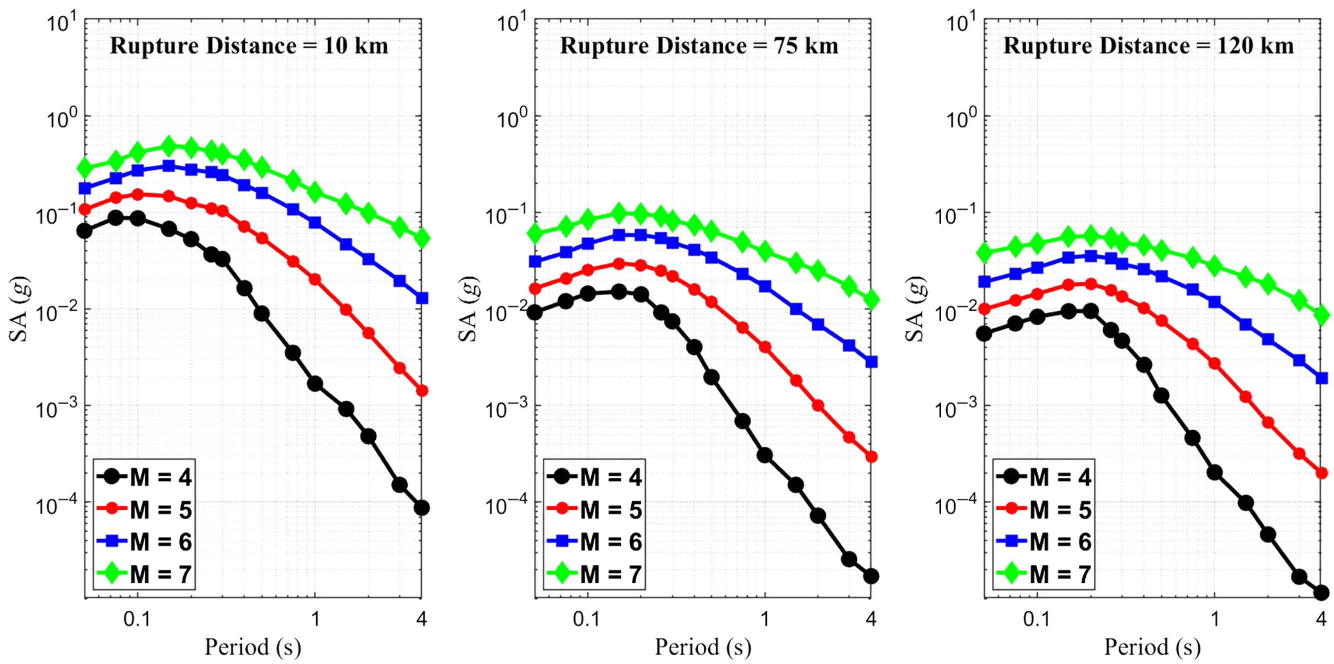

Figure 5. Response spectra predicted by the empirical GMPE developed in this study showing its dependence on magnitude at rupture distances (R_{RUP}) of 10, 75, and 120 km considering $V_{S30} = 360$ m/s. The color version of this figure is available only in the electronic edition.

once they are corrected for the between-event and the site-to-site components of variability up to 4 s. The standard deviations in this figure are given in natural log units so that they can be compared more easily with the standard deviations listed in the literature.

The distribution of between-event, site-to-site, and event-site-corrected residuals, describes the suitability of the source magnitude-scaling, site V_{S30} scaling, and path rupture distance-scaling terms of the functional form, respectively. Figure 7 displays between-event, site-to-site, and

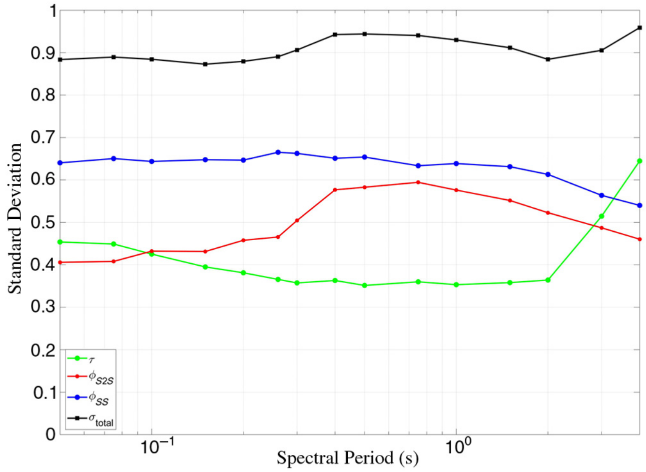

Figure 6. Variation of the between-event standard deviation τ, the site-to-site standard deviation ϕ_{S2S}, the within-event single-site standard deviation ϕ_{SS}, and total aleatory standard deviation as a function of period. The color version of this figure is available only in the electronic edition.

event-site-corrected residuals against predictor variables to explore the validity of our median GMM for PGA and PSA at a period of 1.0 s as a function of the rupture distance, respectively. Error bars represent the mean of binned residuals, along with their 95% confidence intervals. Similarly, Ⓔ Figures S5 and S6 represent residuals as a function of V_{S30} and moment magnitude. The evaluation of these figures shows random distributions of residuals, indicating that there are no obvious biases, and no significant trends and models fit the observations well.

Table 3
Variation of Uncertainties as a Function of Period

T (s)	τ	ϕ_{S2S}	ϕ_{SS}	σ_{total}
0.0000	0.3510	0.3482	0.5680	0.7530
0.0400	0.4256	0.3881	0.6366	0.8585
0.0420	0.4328	0.3889	0.6399	0.8649
0.0440	0.4399	0.3913	0.6409	0.8703
0.0500	0.4471	0.4018	0.6401	0.8781
0.0750	0.4436	0.4027	0.6502	0.8841
0.1000	0.4187	0.4258	0.6422	0.8769
0.1500	0.3836	0.4196	0.6422	0.8577
0.2000	0.3691	0.4190	0.6355	0.8460
0.2600	0.3525	0.3946	0.6480	0.8366
0.3000	0.3410	0.3870	0.6443	0.8253
0.4000	0.3433	0.3956	0.6377	0.8252
0.5000	0.3329	0.3974	0.6407	0.8242
0.7500	0.3359	0.4694	0.6201	0.8472
1.0000	0.3318	0.4957	0.6296	0.8673
1.5000	0.3465	0.5206	0.6270	0.8856
2.0000	0.3612	0.5163	0.6120	0.8784
3.0000	0.5145	0.4871	0.5637	0.9054
4.0000	0.6447	0.4604	0.5400	0.9588

As shown in Figure 7, Ⓔ Figures S5 and S6, and summarized in Table 3, the values of ϕ from the observations are generally higher, likely because of the additional dispersion that results from the large site adjustment. It is also interesting to note that the within-event and single-site standard deviations of the observations are similar to those reported by Rodriguez-Marek *et al.* (2013) for California.

Comparison with Previous Models

Figures 8–10 compare the median predicted values of PSA from the GMM based on this study versus the observed PGA and PSA at periods of $T = 0.2$ and 1.0 s, three magnitude bins centered at $\mathbf{M} = 5$, 6, and 7. In general, there is relatively good agreement between the PSA predictions and the observations, although there are some magnitudes and distances when the comparison is better than others. In these figures, we also plot the distance-scaling (attenuation) characteristics of the GMM developed by Kale *et al.* (2015). The Kale *et al.* (2015) model is developed for the R_{JB} distance metric, and for our GMM we used the closest distance to the fault-rupture surface, represented by the R_{RUP} distance metric. Because the proposed model in the present study is based on R_{RUP}, we converted R_{JB} to R_{RUP} for evaluating the Kale *et al.* (2015) model using the relationships developed by Scherbaum *et al.* (2004).

As shown in Figure 8–10, this study and Kale *et al.* (2015) show relatively similar shapes. For magnitude 5, we do not have data below 10 km, and our model looks different from Kale *et al.* (2015). For magnitude 6, both models exhibit similar shapes with Kale *et al.* (2015) slightly smaller than our model for long distances. For magnitude 7, both models show similar behavior as well. Overall, both the present study and Kale *et al.* (2015) show similar behavior and match the observed data well.

Conclusion

The current empirical GMM is developed for Iran based on a recent strong-motion database (Farajpour *et al.*, 2018). We used a subset of the database containing 1356 records from 208 events, for which the moment magnitude range of the model is $4.8 \le \mathbf{M} \le 7.5$, and the rupture distance R_{RUP} is the closest distance to the rupture plane 400 km. The database includes the variety of fault mechanisms (e.g., strike-slip, normal, and reverse). However, we determined no statistical differences among the variety of fault mechanisms. The predictive model is proposed for PGA, with 5% damped horizontal SA for periods up to 4.0 s for Iran. The equations are developed based on R_{RUP} and $\mathbf{M}$. In the developed GMM, five different regions' earthquakes were considered, but statistical analysis of random effects using a mixed-effect regression procedure showed that the regional differences in the variations estimated in terms of magnitude, distance scaling, and spectral shapes are negligible. A nonlinear site response was implemented in the proposed predictive model.

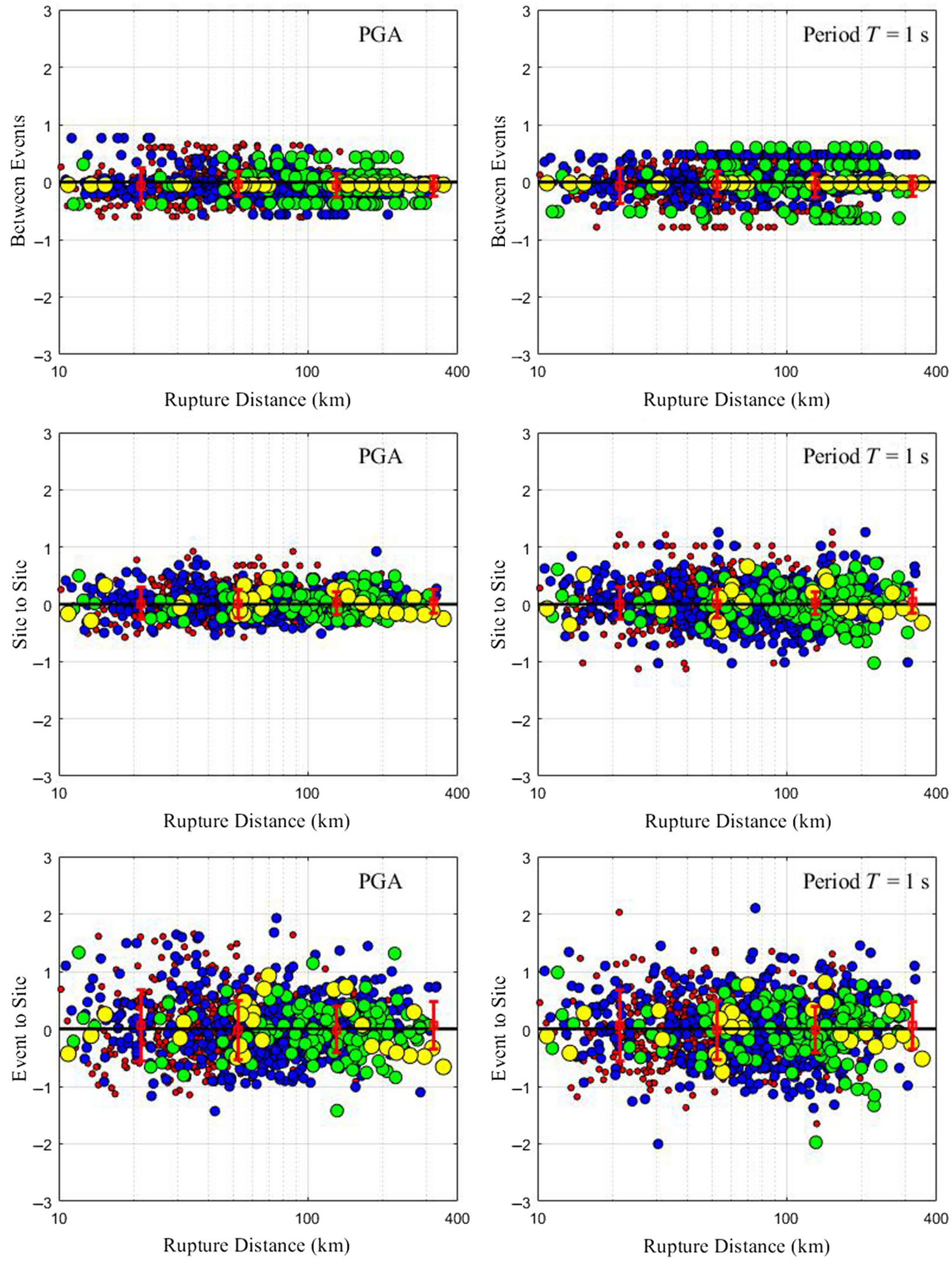

Figure 7. Plots showing the event-to-site, site-to-site, and between-event residual versus distance as a function of rupture distance (R_{RUP}) for PGA and 1 s spectral acceleration. Squares represent the mean of the binned residuals, and the error bar represents ± 1 standard deviation. Size of circles represents the size of the magnitude. The color version of this figure is available only in the electronic edition.

Distribution residuals obtained considering between-event, site-to-site, and event station showed no discernable trends for the proposed GMM. Based on the analyses of residuals, the newly developed set of GMMs is well suited to the database. Our model showed similar characteristics as the Kale *et al.* (2015) model for some distance ranges and some periods and can be used along with Kale *et al.* (2015) and other recent published models to capture the necessary epistemic uncertainties.

Data and Resources

All of the data and models used in this study are available from the cited references.

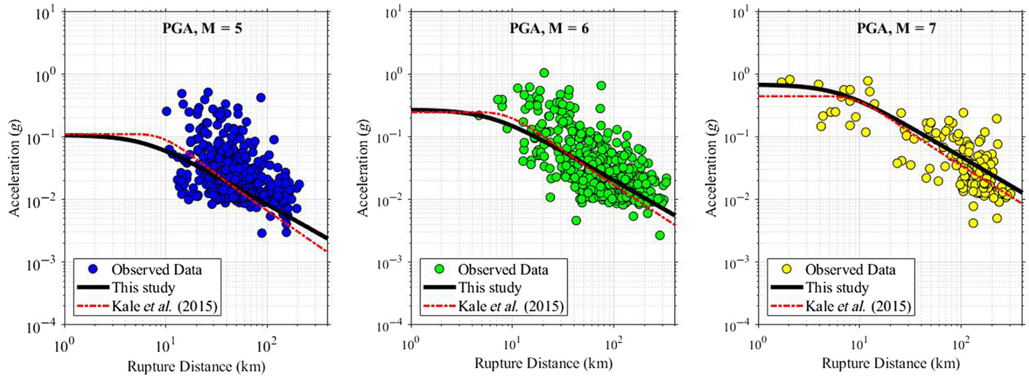

Figure 8. Comparisons of the ground-motion intensity measure (GMIM) predictions based on this study with observations for PGA and three magnitude bins: $\mathbf{M} = 5$ (4.5–5.5), $\mathbf{M} = 5.6$ (5.5–6.5), and $\mathbf{M} = 7.0$ (6.5–7.5). The color version of this figure is available only in the electronic edition.

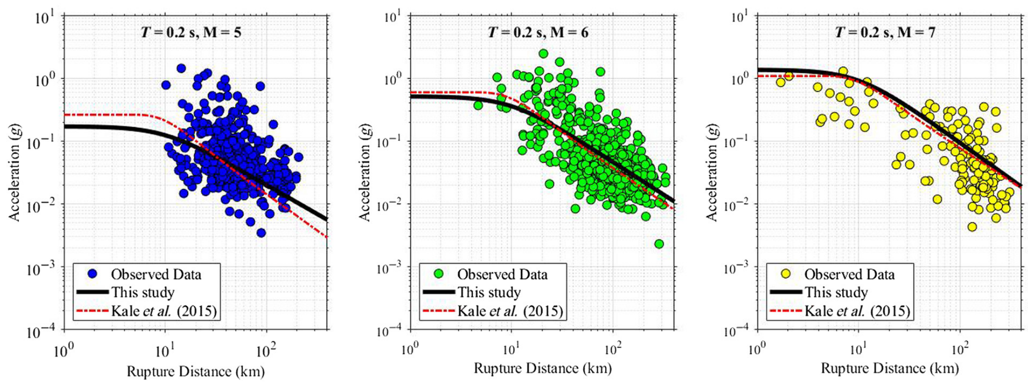

Figure 9. Comparisons of the GMIM predictions based on this study with observations and Kale *et al.* (2015) for spectral periods of 0.2 s and three magnitude bins: $\mathbf{M} = 5$ (4.5–5.5), $\mathbf{M} = 5.6$ (5.5–6.5), and $\mathbf{M} = 7.0$ (6.5–7.5). The color version of this figure is available only in the electronic edition.

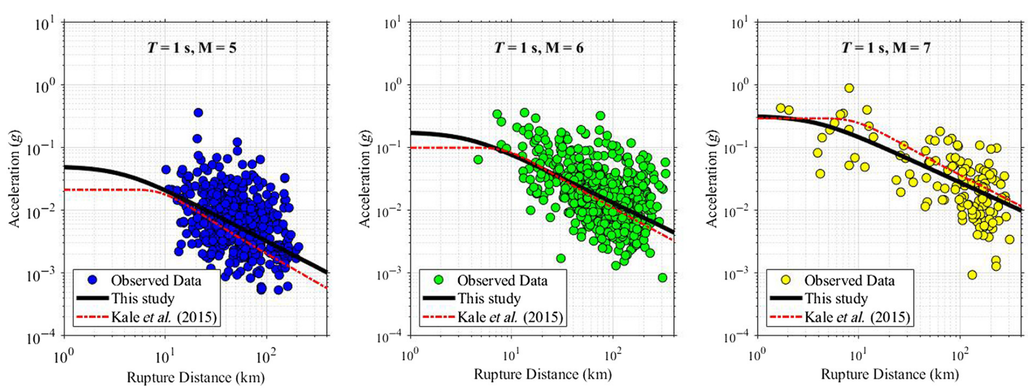

Figure 10. Comparisons of the GMIM predictions based on this study with observations and Kale *et al.* (2015) for spectral periods of 1.0 s and three magnitude bins: $\mathbf{M} = 5$ (4.5–5.5), $\mathbf{M} = 5.6$ (5.5–6.5), and $\mathbf{M} = 7.0$ (6.5–7.5). The color version of this figure is available only in the electronic edition.

Acknowledgments

The authors thank Associate Editor Fabrice Cotton, Hamid Zafarani, Anooshiravan Ansari, and Mohammadreza Ebrahimi for their comments and suggestions. They would also like to thank Benedikt Halldorsson and Dariush Motazedian for their constructive reviews of this article.

References

Abrahamson, N., W. Silva, and R. Kamai (2014). Summary of the ASK14 ground-motion relation for active crustal regions, *Earthq. Spectra* **30,** no. 3, 1025–1055.

Al Atik, L., N. Abrahamson, J. J. Bommer, F. Scherbaum, F. Cotton, and N. Kuehn (2010). The variability of ground-motion prediction models and its components, *Seismol. Res. Lett.* **81,** 794–801.

Berberian, M. (1979). Discussion of the paper A. A. Nowroozi, 1976 Seismotectonic provinces of Iran, *Bull. Seismol. Soc. Am.* **69,** 293–297.

Bozorgnia, Y., N. A. Abrahamson, L. A. Atik, T. D. Ancheta, G. M. Atkinson, J. W. Baker, A. Baltay, D. M. Boore, K. W. Campbell, B. S.-J. Chiou, *et al.* (2014). NGA-West2 research project, *Earthq. Spectra* **30,** no. 3, 973–987.

Building Seismic Safety Council (BSSC) (2009). NEHRP recommended seismic provisions for new buildings and other structures: part 1, provisions, Federal Emergency Management Agency (P-750), Washington, D.C.

Campbell, K. W., and Y. Bozorgnia (2013). NGA-West2 Campbell–Bozorgnia ground motion model for the horizontal components of PGA, PGV, and 5%-damped elastic pseudo-acceleration response spectra for periods ranging from 0.01 to 10 sec, *PEER Report 2013/06*, Pacific Earthquake Engineering Research Center, University of California, Berkeley, 238 pp.

Chandra, V. J., G. McWhorten, and A. Nowroozi (1979). Attenuation of intensities in Iran, *Bull. Seismol. Soc. Am.* **69,** 237–250.

Douglas, J. (2004). An investigation of analysis of variance as a tool for exploring regional differences in strong ground motions, *J. Seismol.* **8,** 485–496.

Farajpour, Z., M. Zare, S. Pezeshk, A. Ansari, and E. Farzanegan (2018). Near-source strong motion database catalog of Iran, *Arab. J. Geosci.* **11,** no. 4, 80.

Ghasemi, H., M. Zare, Y. Fukushima, and K. Koketsu (2009). An empirical spectral ground-motion model for Iran, *J. Seismol.* **13,** 499–515.

Hamzehloo, H., and M. Mahood (2012). Ground-motion attenuation relationship for east central Iran, *Bull. Seismol. Soc. Am.* **102,** no. 6, 2677–2684.

Kaklamanos, J., L. G. Baise, and D. M. Boore (2011). Estimating unknown input parameters when implementing the NGA ground-motion prediction equations in engineering practice, *Earthq. Spectra* **27,** 1219–1235.

Kale, O., S. Akkar, A. Ansari, and H. Hamzehloo (2015). A ground-motion predictive model for Iran and Turkey for horizontal PGA, PGV, and 5%-damped response spectrum: Investigation of possible regional effects, *Bull. Seismol. Soc. Am.* **105,** 963–980.

Kamai, R., N. A. Abrahamson, and W. J. Silva (2013). Nonlinear horizontal site response for the NGA-West2 project, *Report PEER 2013/12*, Pacific Earthquake Engineering Research Center, University of California, Berkeley, 97 pp.

Kotha, S. R., D. Bindi, and F. Cotton (2016). Partially non-ergodic region-specific GMPE for Europe and Middle-East, *Bull. Earthq. Eng.* **14,** 1245–1263.

Lindstrom, M. J., and D. M. Bates (1990). Nonlinear mixed effects models for repeated measures data, *Biometrics* **46,** 673–687.

MathWorks Inc. (2017). *MATLAB and Statistics and Machine Learning Toolbox, Release 2017a*, The MathWorks Inc., Natick, Massachusetts, 519 pp.

Mirzaei, N., G. Mengtan, and C. Yuntai (1998). Seismic source regionalization for seismic zoning of Iran: Major seismotectonic provinces, *J. Earthq. Pred. Res.* **7,** 465–495.

Nowroozi, A. A. (1976). Seismotectonic provinces of Iran, *Bull. Seismol. Soc. Am.* **66,** 1249–1276.

Nowroozi, A. A. (2005). Attenuation relations for peak horizontal and vertical accelerations of earthquake ground motion in Iran: A preliminary analysis, *J. Seismol. Earthq. Eng.* **7,** no. 2, 109–128.

Ramazi, H. R., and V. Schenk (1994). Preliminary results obtained from strong ground motion analyses of Iranian earthquakes, *Proc. of the XXIV General Assembly of the European Seismological Commission, III*, Athens, Greece, 19–24 September, 1762–1770.

Rodriguez-Marek, A., F. Cotton, N. A. Abrahamson, S. Akkar, L. Al Atik, B. Edwards, G. A. Montalva, and H. M. Dawood (2013). A model for single-station standard deviation using data from various tectonic regions, *Bull. Seismol. Soc. Am.* **103,** 3149–3163.

Sadeghi, H., A. Shooshtari, and M. Jaladat (2010). Prediction of horizontal response spectra of strong ground motions in Iran and its regions, *Proc. of the Ninth U.S. National and 10th Canadian Conf. on Earthquake Engineering: Reaching Beyond Borders*, Toronto, Canada, 25–29 July, Paper Number 861.

Saffari, H., Y. Kuwata, S. Takada, and A. Mahdavian (2012). Updated PGA, PGV, and spectral acceleration attenuation relations for Iran, *Earthq. Spectra* **28,** 257–276.

Scherbaum, F., J. Schmedes, and F. Cotton (2004). On the conversion of source-to-site distance measures for extended earthquake source models, *Bull. Seismol. Soc. Am.* **94,** 1053–1069.

Sedaghati, F., and S. Pezeshk (2017). Partially nonergodic empirical ground-motion models for predicting horizontal and vertical PGV, PGA, and 5% damped linear acceleration response spectra using data from the Iranian plateau, *Bull. Seismol. Soc. Am.* **107,** no. 2, 934–948.

Seyhan, E., and J. P. Stewart (2014). Semi-empirical nonlinear site amplification from NGA-West2 data and simulations, *Earthq. Spectra* **30,** no. 3, 1241–1256.

Silva, W. J. (2005). *Site Response Simulations for the NGA Project*, Pacific Engineering and Analysis, El Cerrito, California.

Soghrat, M. R., N. Khaji, and H. Zafarani (2012). Simulation of strong ground motion in northern Iran using the specific barrier model, *Geophys. J. Int.* **188,** no. 2, 645–679.

Stoklin, J. (1968). Structural history and tectonics of Iran, *Am. Assoc. Petrol. Geol. Bull.* **52,** 1229–1258.

Takin, M. (1972). Iranian geology and continental drift in the Middle East, *Nature* **235,** 147–150.

Tavakoli, B., and M. Ghafory-Ashtiany (1999). Seismic hazard assessment of Iran, *Ann. Geofisc.* **42,** 1013–1021.

Wald, D. J., and T. I. Allen (2007). Topographic slope as a proxy for seismic site conditions and amplification, *Bull. Seismol. Soc. Am.* **97,** no. 5, 1379–1395.

Wald, D. J., P. S. Earle, and V. Quitoriano (2004). Topographic slope as a proxy for seismic site amplification correction, *AGU Fall Meeting Abstracts*, Abstract ID S42A–01.

Walling, M., W. J. Silva, and N. A. Abrahamson (2008). Non-linear site amplification factors for constraining the NGA models, *Earthq. Spectra* **24,** 243–255.

Wells, D. L., and K. J. Coppersmith (1994). New empirical relationships among magnitude, rupture length, rupture width, rupture area, and surface displacement, *Bull. Seismol. Soc. Am.* **84,** no. 4, 974–1002.

Zafarani, H., and M. Soghrat (2012). Simulation of ground motion in the Zagros region of Iran using the specific barrier model and the stochastic method, *Bull. Seismol. Soc. Am.* **102,** no. 5, 2031–2045.

Zafarani, H., M. Mousavi, A. S. Noorzad, and A. Ansari (2008). Calibration of the specific barrier model to Iranian plateau earthquakes and development of physically based attenuation relationships for Iran, *Soil Dynam. Earthq. Eng.* **28,** no. 7, 550–576.

Zafarani, H., L. Luzi, G. Lanzano, and M. R. Soghrat (2017). Empirical equations for the prediction of PGA and pseudo spectral accelerations using Iranian strong-motion data, *J. Seismol.* **22,** no. 1, 263–285, doi: 10.1007/s10950-017-9704-y.

Zare, M., M. Ghafory-Ashtiany, and P.-Y. Bard (1999). Attenuation law for the strong-motions in Iran, *Proc. of the Third International Conf. on*

Seismology and Earthquake Engineering, Tehran, Iran, Vol. 1**,** 345–354.

Zare, M., and S. Sabzali (2006). Spectral attenuation of strong motions in Iran, *Proc. of Third International Symposium on the Effects of Surface Geology on Seismic Motion*, Grenoble, France, 30 August–1 September, Vol. 1, Paper Number 146, 749–758.

International Institute of Earthquake Engineering and Seismology
Tehran, Iran
zoya.farajpour@gmail.com
mehdi.zare.iran@gmail.com
(Z.F., M.Z.)

Department of Civil Engineering
The University of Memphis
Memphis, Tennessee
spezeshk@memphis.edu
(S.P.)

Manuscript received 8 May 2018;
Published Online 19 February 2019